crystals

MDPI

Article

Electron Transport Layer-Free Ruddlesden–Popper Two-Dimensional Perovskite Solar Cells Enabled by Tuning the Work Function of Fluorine-Doped Tin Oxide Electrodes

Ningfei Dong [1], Haosu Zhou [2], Lei Wang [3] and Zhihai Liu [1,*]

[1] School of Physics and Electronic Information, Yantai University, Yantai 264005, China
[2] Shanghai Spaceflight Institute of TT&C and Telecommunication, Shanghai 201109, China
[3] School of Artificial Intelligence, Beijing Technology and Business University, Beijing 100048, China
* Correspondence: zhliu@ytu.edu.cn

Abstract: Organic–inorganic halide two-dimensional (2D) layered perovskites have been demonstrated to have better environmental stability than conventional three-dimensional perovskites. In this study, we investigate the fabrication of electron transport layer (ETL)-free Ruddlesden–Popper 2D perovskite solar cells (PSCs) by tuning the work function of a fluorine-doped tin oxide (FTO) electrode. With the deposition of polyethylenimine (PEIE) onto its surface, the work function of the FTO electrode could be raised from −4.72 to −4.08 eV, which is more suitable for electron extraction from the perovskite absorber. Using this technique, the ETL-free 2D PSCs exhibited an excellent power conversion efficiency (PCE) of 12.7% (on average), which is substantially higher than that of PSCs fabricated on a pristine FTO electrode (9.6%). Compared with the PSCs using TiO_2, the ETL-free PSCs could be fabricated under a low processing temperature of 100 °C with excellent long-term stability. After 15 days, the FTO/PEIE-based ETL-free PSCs showed a PCE degradation of 16%, which is significantly lower than that of the TiO_2-based case (29%). The best-performing PSC using a FTO/PEIE cathode showed a high PCE of 13.0%, with a small hysteresis degree of 2.3%.

Keywords: 2D perovskite; ETL-free; work function; power conversion efficiency; stability

Citation: Dong, N.; Zhou, H.; Wang, L.; Liu, Z. Electron Transport Layer-Free Ruddlesden–Popper Two-Dimensional Perovskite Solar Cells Enabled by Tuning the Work Function of Fluorine-Doped Tin Oxide Electrodes. *Crystals* **2022**, *12*, 1090. https://doi.org/10.3390/cryst12081090

Academic Editor: Sawanta S. Mali

Received: 13 July 2022
Accepted: 1 August 2022
Published: 4 August 2022

1. Introduction

Recently, organic–inorganic hybrid metal halide perovskite materials have been intensively studied because of their unique properties, for instance, high light absorption coefficient, low cost, light weight, direct band gaps, and simple solution processability [1–3]. As a result, perovskite solar cells (PSCs) have been rapidly developed, and their power conversion efficiency (PCE) has significantly improved from 3.8% to 25.7% [4,5]. Although PSCs showed comparable PCEs to silicon solar cells, the devices also suffered from several disadvantages. For example, conventional $MAPbX_3$ (MA = CH_3NH_3, X = halogen) perovskite can be gradually hydrated by water and decomposed into PbI_2 in air [6], inducing poor environmental stability for the PSCs. Hence, the long-term stability of the PSCs needs to be enhanced, which is an essential requirement for commercialization [7]. To fully solve this problem, finding new perovskite absorbers with higher intrinsic stability is important. For the past few years, two-dimensional (2D) or quasi 2D perovskite absorbers have been investigated and have displayed great potential for replacing $MAPbX_3$ in PSCs, which show an improved stability. Specifically, Ruddlesden–Popper-type 2D perovskites (e.g., $(BA)_2(MA)_{n-1}Pb_nI_{3n+1}$, BA stands for $CH_3(CH_2)_3NH_3$), and n is an integer) showed tunable and direct band gaps of about 1.5–2.2 eV [8,9], which is similar with that of conventional 3D perovskites.

PSCs are usually fabricated into a standard layer-by-layer structure, with perovskite absorbers sandwiched by the charge transport layers [2,10]. For conventional n-i-p PSCs, 2,2′,7,7′-tetrakis-(*N*,*N*-di-*p*-methoxyphenylamine)-9,9′-spirobifluorene (spiro-OMeTAD)

has been widely used to form the hole transport layer (HTL) [10]. In the case of the electron transport layer (ETL), TiO_2 has been frequently prepared with a planar or mesoporous structure, which showed good chemical stability [10,11]. However, sintering the TiO_2 layers requires a high temperature of about 500 °C in a furnace, which is detrimental to the roll-to-roll production of the PSCs [12]. Moreover, the photocatalytic effect of TiO_2 would gradually decompose perovskite into PbI_2 under the exposure of ultraviolet (UV) light [13], which further limits the long-term stability of the PSCs. As a result, some other ETL materials have been investigated for replacing TiO_2 in PSCs. For example, n-type ZnO and SnO_2 have been developed as the ETLs in the fabrication of PSCs, which could be processed at a lower temperature of 150–200 °C [14–16]. Compared with the PSCs using TiO_2, the ZnO- or SnO_2-based devices showed comparable PCEs and improved stability. Wojciechowski et al. reported the use of C_{60} as an efficient n-type compact layer for replacing TiO_2, which simultaneously improved the PCE and stability of the PSCs [17]. Zhang et al. inserted a thin indacenodithiophene (IDIC) layer between the cathode and perovskite absorber, which avoided the use of TiO_2 in PSCs. Due to the improved perovskite quality and electron extraction property, the IDIC-based PSCs showed a champion PCE of 19.1% and significantly improved device stability [18]. Recently, ETL-free n-i-p PSCs have also been investigated, which could be fabricated under a low processing temperature of about 100 °C [19]. With some treatment or surface modification to the fluorine-doped tin oxide (FTO) electrode, the 3D perovskite-based ETL-free PSCs exhibited excellent PCEs of 10.1–21.1% and enhanced stability [19–22]. However, there are very few reports on the investigation of ETL-free PSCs based on 2D perovskite absorbers. Considering the problem of using TiO_2 and the stability issue of 2D perovskites, it is very important to research the performance of ETL-free 2D PSCs.

In this study, we fabricated ETL-free 2D n-i-p PSCs using Ruddlesden–Popper $(BA)_2(MA)_3Pb_4I_{13}$ as the perovskite absorber, which can be processed under a low temperature of 100 °C. By coating a thin polyethylenimine (PEIE) layer onto the surface, the work function of the FTO electrode can be tuned from −4.72 to −4.08 eV. The raised working function is beneficial for reducing the electron transporting barrier, which has significant effects on the performance of PSCs. Consequently, the ETL-free 2D PSCs using cathode of FTO/PEIE exhibited an average PCE of 12.7%, which is much higher than that of the PSCs fabricated on bare FTO (9.6%). Although the PCE is slightly lower than that of conventional TiO_2-based PSCs (13.5%), the long-term stability of the PSCs has been dramatically enhanced. With a duration test of 15 days in ambient conditions, the PCE degradation of the ETL-free PSCs is 16%, which is significantly lower than that of the TiO_2-based case (29%). The best performing PSC using FTO/PEIE cathode presented a high PCE of 13.0%, which showed a stable power output and negligible hysteresis. Our results indicate that the use of PEIE-modified FTO is a simple but efficient way to fabricate ETL-free 2D PSCs with high PCE and stability.

2. Experimental Section

2.1. Device Fabrication

Bis(trifluoromethane) sulfonamide lithium salt, 4-tert-butylpyridine (*t*BP), PEIE, 2-methoxyethanol, acetonitrile, Butylammonium iodide (BAI), chlorobenzene (CB), *N*,*N*-dimethylformamide (DMF) and dimethyl sulfoxide (DMSO) were purchased from Sigma-Aldrich (St. Louis, MO, USA). The pattern FTO glasses and PbI_2 were purchased from Advanced Election Technology Co., Ltd. Methylammonium iodide (MAI) and spiro-OMeTAD were obtained from Xi'an Polymer Light Technology Corp. (Xi'an , China). Figure 1a shows the schematic of our ETL-free 2D PSCs, which were fabricated into a structure of glass/FTO/PEIE/$(BA)_2(MA)_3Pb_4I_{13}$/spiro-OMeTAD/Au. The perovskite precursor solution was prepared by dissolving BAI, MAI, and PbI_2 (with a molar ratio of 2:3:4) in a mix-solvent of DMF and DMSO at a total concentration of 40 wt%. For spiro-OMeTAD solution, 150 mg spiro-OMeTAD, 56 µL *t*BP, and 36 µL solution of lithium salt (0.52 g mL^{-1} in acetonitrile) were mixed in 2 mL CB. First, PEIE solution (0.4 wt% in

2-methoxyethanol) was spin-coated onto the pre-cleaned FTO glasses at 5000 rpm, followed by a thermal annealing at 100 °C for 10 min. Then, the perovskite precursor solution was spin-casted onto the FTO/PEIE cathode at 4200 rpm under the protection of N_2 in the glovebox. The $(BA)_2(MA)_3Pb_4I_{13}$ perovskite films formed after being heated at 100 °C for 10 min. Under the same environment, the spiro-OMeTAD solution was spin-coated onto the pre-formed $(BA)_2(MA)_3Pb_4I_{13}$, and then thermally annealed at 80 °C. For control PSCs, the operation of coating PEIE was skipped. For TiO_2 based PSCs, the preparation of TiO_2 ETL followed that in our previous study [23]. The fabrication was finished by depositing about 100 nm Au onto the spiro-OMeTAD films using a thermal evaporation system under a low pressure of 10^{-4} Pa. As indicated from the FTO pattern and shadow mask, the effective working area of all the PSCs in this study is determined to be 0.1 cm^2.

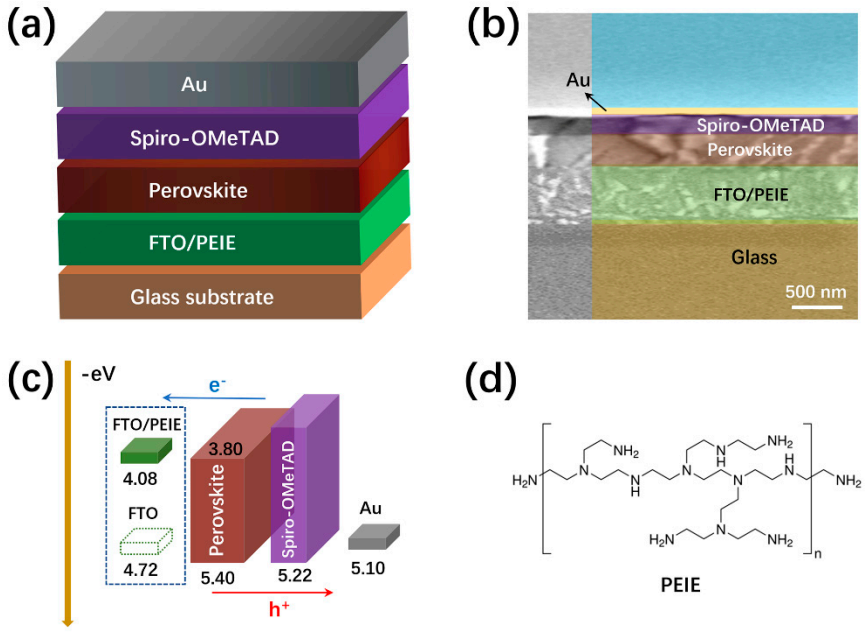

Figure 1. (**a**) Schematic device structure of the PSCs; (**b**) Cross-sectional SEM image of a PSC; (**c**) schematic energy levels of the functional layers involved in the PSCs; (**d**) chemical structure of PEIE.

2.2. Characterization

The current density–voltage (*J*–*V*) characteristic performances of the PSCs were measured under the irradiation of AM1.5 (light intensity of 100 mW cm^{-2}). The incident photon-to-current efficiency (IPCE) responses of the PSCs were collected by using an IPCE measurement system (Solar Cell Scan 100, Zolix, Beijing, China) for a wavelength of 300–800 nm. The work functions of the electrodes were measured using an ultraviolet photoelectron spectroscope (UPS) based on a radiation line of He I (21.22 eV). The crystallinity of the perovskite film was detected using an X-ray diffractometer (XRD, Panalytical, Almemo, The Netherlands). The cross-sectional image of the PSCs and top-view images of the perovskite surface were measured using a scanning electron microscope (SEM, JEOL, Akishima, Japan) under an acceleration voltage of 15 kV. Surface morphologies of the FTO substrates were obtained by using a tapping mode atomic force microscopy (AFM, Veeco, Plainview, NY, USA). The photoluminescence (PL) spectra of the films were acquired using a spectrometer of FLS920 (Edinburgh Instruments, Livingston, UK) under the excitation wavelength of 372 nm. The electrochemical impedance spectroscopy (EIS) spectra of the PSCs were measured and analyzed using an electrochemical work station (CH Instruments, Bee Cave, TX, USA).

3. Results and Discussion

Figure 1b shows the cross-sectional SEM image of the ETL-free PSCs, which indicates a well-connected layer-by-layer structure. From the SEM image, the $(BA)_2(MA)_3Pb_4I_{13}$ perovskite and spiro-OMeTAD layers showed standard thicknesses of approximately 420 and 230 nm, respectively. The PEIE was inserted between the perovskite and FTO electrodes, which would tune the energy level of the FTO. The energy levels of all the functional layers were schematically shown in Figure 1c, which displays the charge generation and transport process of PSCs. As can be seen, charge carriers can be generated in the perovskite absorber under sunlight with holes transported through spiro-OMeTAD to Au anode and electrons transported to an FTO or FTO/PEIE cathode [10]. The chemical structure of PEIE is illustrated in Figure 1d, which indicates many amine groups in the molecule.

As shown in the UPS spectra in Figure 2a, a bare FTO electrode has a work function of −4.72 eV, which is a typical value shown in previous studies [10,24]. As indicated in Figure 1c, the energy level of the lowest unoccupied molecular orbital (LUMO) for $(BA)_2(MA)_3Pb_4I_{13}$ perovskite is about −3.80 eV [9], which is much higher than that of FTO. As a result, an energy barrier may be formed, which may further limit the electron transport from the $(BA)_2(MA)_3Pb_4I_{13}$ film to FTO cathode [23]. The PEIE modified FTO showed a raised work energy level of −4.08 eV, which lies on the slightly lower position with the LUMO of perovskite layer. Consequently, the generated electrons would freely flow from perovskite to FTO/PEIE, which is beneficial for charge dissociation [25]. As indicated from Figure 1d, the large amount of amine groups of PEIE molecules would induce the formation of surface dipoles on those FTO electrodes [26], which further tuned the work function of FTO to −4.08 eV. As shown in Figure 2b, bare FTO and FTO/PEIE electrodes both showed a high transparency of more than 80% for a broad wavelength range of 370−790 nm. The high transmittance further ensures the sufficient light absorption of $(BA)_2(MA)_3Pb_4I_{13}$ perovskite. Figure S1 (see Supplementary Materials) shows the contact angles for the surfaces of bare FTO and FTO/PEIE electrodes. Upon using PEIE, the contact angle decreased from 66° to 45°, indicating a reduced hydrophobic property. As indicated in a previous study, increasing the hydrophilic property of the underlayer is beneficial for forming a more uniform perovskite film [27]. Surface morphologies of the bare FTO and FTO/PEIE electrodes are shown in Figure 2c,d. The bare FTO electrode showed a rough surface morphology, which has a large root mean square (RMS) roughness of 6.7 nm. After being coated by PEIE, the surface of FTO becomes more uniform, with the RMS roughness reduced to 5.2 nm. A smoother morphology of the bottom layer is beneficial for forming ohmic contact and lowering contact resistance with the upper perovskite, which will be discussed later.

The solar performance of PSCs is greatly affected by the quality of perovskite films, which is highly related to light absorption, charge generation, and carrier transportation [10]. Figure 3 shows the UV–vis absorption, XRD, and SEM image of the prepared perovskite film on FTO/PEIE substrate, which measure the $(BA)_2(MA)_3Pb_4I_{13}$ quality. Figure 3a demonstrates a typical and broad light absorption range at 400–800 nm for the $(BA)_2(MA)_3Pb_4I_{13}$ perovskite film with a specific absorption peak at 610 nm, which is highly related to the band structure of the $(BA)_2(MA)_3Pb_4I_{13}$ perovskite (Figure 1c). The shape of the absorption curve is in agreement with those in previous reports [9,28]. The XRD spectrum in Figure 3b shows two significant peaks at 14.2° and 28.4°, which represent the crystallographic (111) and (202) planes for the Ruddlesden–Popper perovskite film. The obvious and sharp characteristic peaks demonstrate the high crystallinity of the $(BA)_2(MA)_3Pb_4I_{13}$ film. The SEM images in Figure 3c,d indicate a fully covered and uniform morphology for the perovskite layer. In Figure 3d, the perovskite grains show a 2D morphology with diameters between 0.8 and 2 μm, which is close to those produced in previous reports [28–30]. The absorption, XRD, and SEM results demonstrate a well-prepared $(BA)_2(MA)_3Pb_4I_{13}$ film on FTO/PEIE substrate with high quality, which is similar to that on bare FTO.

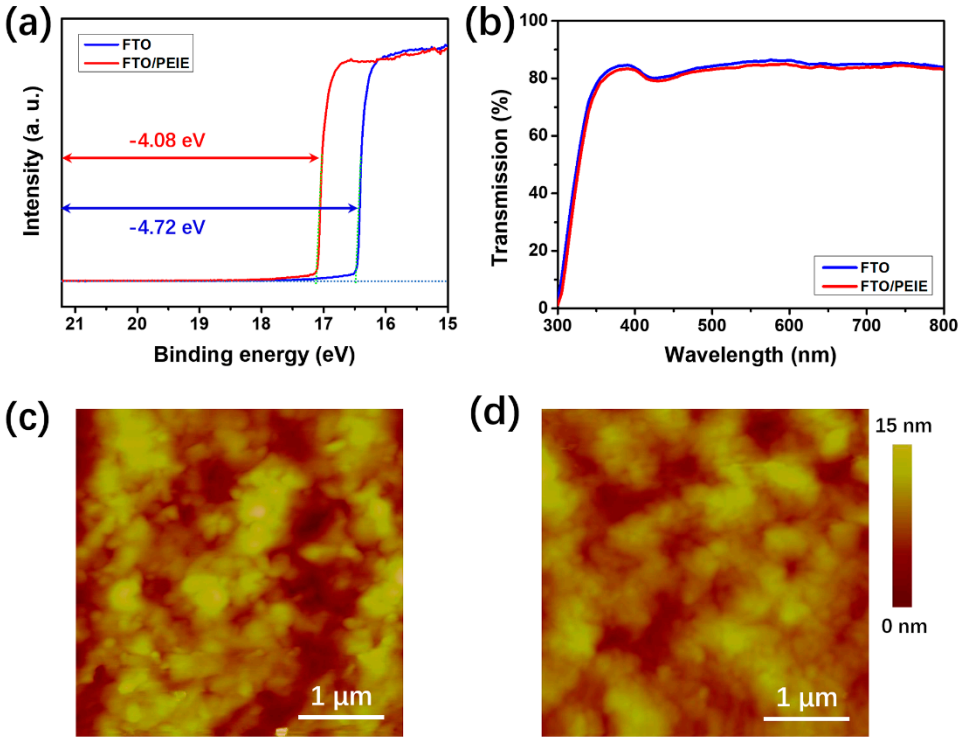

Figure 2. UPS (**a**) and transmission (**b**) spectra of bare FTO and FTO/PEIE electrodes; AFM height images of bare FTO (**c**) and FTO/PEIE (**d**) electrodes.

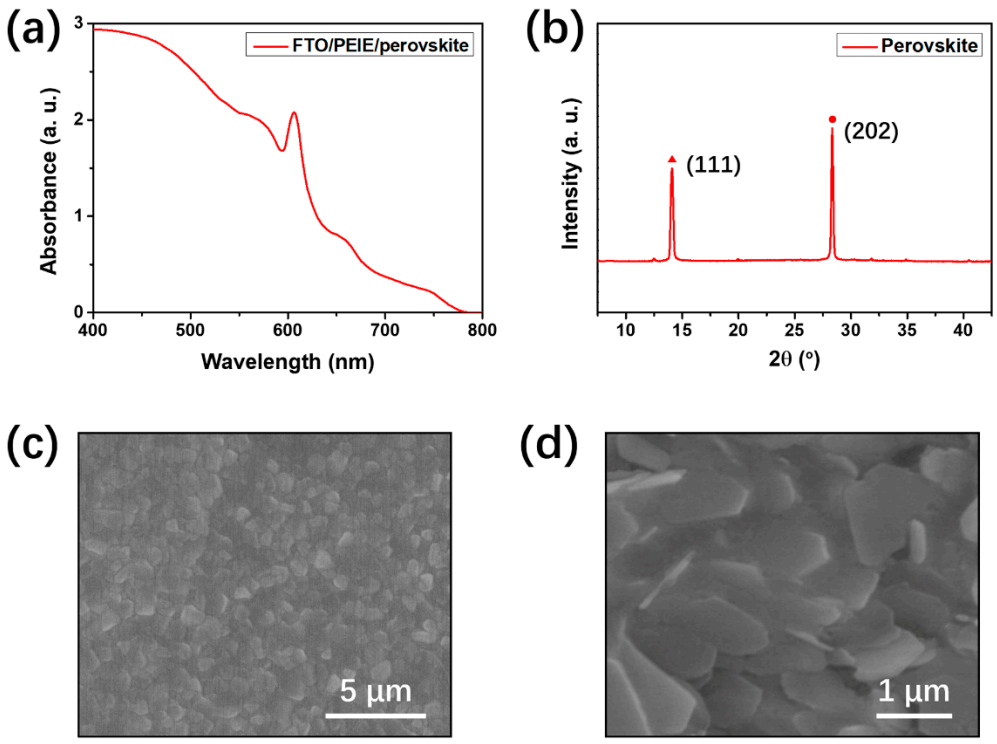

Figure 3. UV−vis spectrum (**a**) and XRD pattern (**b**) of the prepared $(BA)_2(MA)_3Pb_4I_{13}$ perovskite film; Low (**c**) and high (**d**) magnified SEM images of the prepared $(BA)_2(MA)_3Pb_4I_{13}$ perovskite layer on FTO/PEIE substrate.

Figure 4a displays the *J*–*V* characteristics of the PSCs fabricated on bare FTO and FTO/PEIE substrates with all the parameters summarized in Table 1. By forward scanning,

the PSCs on bare FTO showed an average PCE of 9.6%, with a low short-circuit current density (J_{sc}) of 16.7 mA cm^{-2}, a fill factor (FF) of 57.2% and an open-circuit voltage (V_{oc}) of 1.01 V. By coating PEIE onto the FTO electrode, the performance of the PSCs was significantly improved, with a high of 12.7%. The improved PCE was mainly induced by the largely enhanced J_{sc} (18.5 mA cm^{-2}) and FF (66.8%). V_{oc} of the FTO/PEIE-based PSCs was slightly improved to 1.03 V. As shown in Figure S2 (see Supplementary Materials), the regular PSCs using TiO_2 showed a PCE of 13.5%, with a higher J_{sc} (19.4 mA cm^{-2}) and FF (67.5%). Although the FTO/PEIE-based ETL-free PSCs showed slightly lower PCE, the total processing temperature can be dramatically lowered from 500 °C to 100 °C. Figure S3 (see Supplementary Materials) shows the real PCE values for 16 devices in each group, indicating a small PCE variation for the three kinds of PSCs. Figure 4b presents the IPCE spectra of the PSCs fabricated on bare FTO and FTO/PEIE substrates, which shows a photon-to-electron response at 300–800 nm. The integrated J_{sc} from the IPCE responses are 16.3 and 18.2 mA cm^{-2} for PSCs fabricated on bare FTO and FTO/PEIE, which are only 1.6–2.4% different from the values in the *J*–*V* characteristics. As shown in Figure 4c, the best-performing PSC on FTO/PEIE exhibited a high PCE of 13.0%, which is comparable to $(BA)_2(MA)_3Pb_4I_{13}$-based 2D PSCs with ETL [28–31]. Under reverse scan, a slightly higher PCE of 13.3% was obtained, indicating a hysteresis degree of 2.3%. From the reverse *J*–*V* performance, the hysteresis was caused by the slightly higher V_{oc} and FF. The steady-state outputs (PCE and current density) for the best-performing device are shown in Figure 4d, which demonstrates a stable current density (16.0 to 16.3 mA cm^{-2}) and PCE (12.3–12.5%) for a period of 300 s. The best PSC on bare FTO showed a current density of 11.2–11.5 mA cm^{-2}, which leads to a PCE range of 9.1–9.4%.

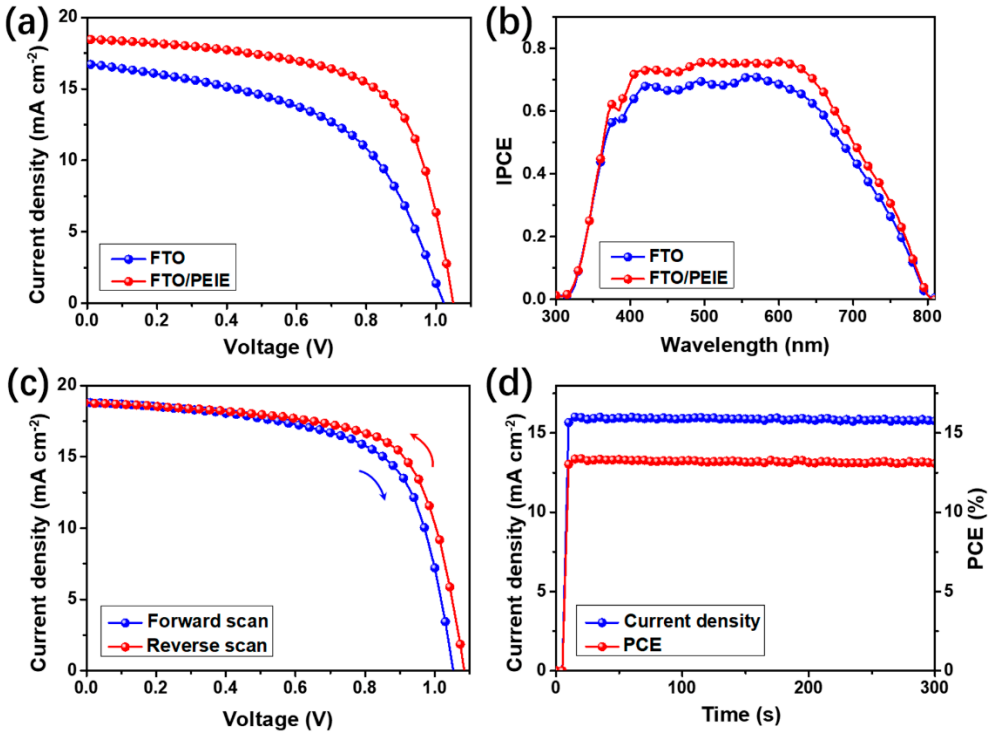

Figure 4. *J*–*V* characteristics under forward scan (**a**) and IPCE spectra (**b**) of the PSCs fabricated on bare FTO and FTO/PEIE as the cathodes; (**c**) *J*–*V* characteristics of a best performing PSC fabricated on FTO/PEIE under forward and reverse scans; (**d**) current density and PCE as a function of time for the best performing PSC with an applied bias of 0.76 V.

Table 1. Solar parameters (extracted from 16 individual devices) of the PSCs fabricated on bare FTO, FTO/PEIE and FTO/TiO_2.

Device Configuration	V_{oc} (V)	J_{sc} (mA cm^{-2})	FF (%)	Average PCE (%)	Best PCE (%)
FTO/perovskite	1.01 ± 0.01	16.7 ± 0.3	57.2 ± 1.3	9.6 ± 0.3	9.9
FTO/PEIE/perovskite	1.03 ± 0.01	18.5 ± 0.2	66.8 ± 1.2	12.7 ± 0.3	13.0
FTO/TiO_2/perovskite	1.03 ± 0.01	19.4 ± 0.3	67.5 ± 1.3	13.5 ± 0.3	13.8

To identify the electron transport property upon using PEIE, we detected the PL and the time-resolved-PL (TR-PL) performance of bare perovskite, perovskite on FTO, and perovskite on FTO/PEIE substrates. As shown in Figure 5a, the bare $(BA)_2(MA)_3Pb_4I_{13}$ perovskite on glass substrate displays an obvious PL signal at 778 nm, which is consistent with those in previous works [29,31]. The PL peak for perovskite on pristine FTO was approximately 60% lower than that of bare perovskite, which was quenched by the FTO electrode. When using PEIE, the PL signal was reduced by 87%, indicating a strong quenching effect of FTO/PEIE on perovskite. This is highly related to the efficient charge transport, which is induced by the improved alignment of energy bands. As indicated in Figure 1c, the FTO/PEIE cathode has a higher work function of −4.08 eV, a suitable value for electron transport from the LUMO of perovskite [23]. Hence, the generated excitons in the perovskite layer would be significantly quenched when using FTO/PEIE at the bottom. Figure 5b shows the TR-PL responses of perovskite on FTO and FTO/PEIE substrates, which indicates a shortened lifetime for the PL signal upon using PEIE. With a bi-exponential fitting to these points, the lifetimes of the PL responses can be calculated for perovskite films on FTO (135 ns) and FTO/PEIE (86 ns) substrates. The shorter PL lifetime demonstrates the faster quenching effect of excitons for the use of FTO/PEIE, which reduced the electron transporting barrier [28].

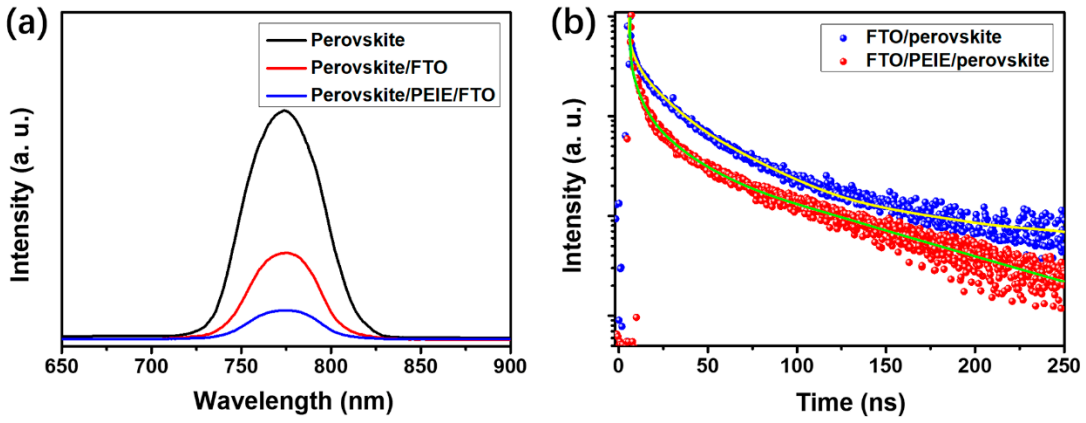

Figure 5. PL (**a**) spectra and time resolved-PL (TR-PL) (**b**) responses for devices of perovskite on glass, perovskite on pristine FTO and perovskite on FTO/PEIE substrates.

The electron transport process of the PSCs can also be characterized by measuring the EIS spectra and light intensity-dependent outputs. As shown in Figure 6a, the EIS curves of the PSCs usually consist of two frequency ranges with the left part (high frequency) corresponding to series resistance (R_s) and the right part (low frequency) reflecting charge-transfer resistance (R_{ct}) [32]. In PSCs, usually R_s is highly related to the contact resistance of different functional layers and R_{ct} can be used to describe the resistance of the charge transport process [33–35]. When fitting the EIS curves with the inner equivalent circuit, the R_{ct} of PSCs fabricated on FTO/PEIE is 368 Ω, which is smaller than that of PSCs fabricated on bare FTO (552 Ω). The decreased R_{ct} could explain the enhanced charge transport property of the PSCs with the cathode of FTO/PEIE, which could be attributed to the improved alignment of energy bands and reduced contact resistance between the cathode and perovskite layers [33–35]. Figure 6b illustrates the relationship between J_{sc} and

light intensity (varied from 10 to 100 mW cm^{-2}) for the PSCs fabricated on bare FTO and FTO/PEIE. The FTO/PEIE-based PSCs exhibited a calculated slope of 0.98, whereas the PSCs on bare FTO represented a lower slope of 0.92. The higher slope, which is close to the ideal value of 1, reveals a suppressed bi-molecular charge recombination of the PSCs when coating PEIE onto the FTO electrode [36]. The suppressed bi-molecular recombination may be induced by the facilitated electron transport to the FTO/PEIE cathode, leading to a weaker electron-hole recombination between the cathode and perovskite [31]. The higher J_{sc} of PSCs fabricated on bare FTO may be induced by the slightly higher transparency of FTO substrate (Figure 2b). The dependence of V_{oc} and light intensity of the PSCs using bare FTO and FTO/PEIE is shown in Figure 6c, which indicates different slopes for two devices. The bare FTO-based PSCs show a steep slope of 1.72 kT/q, where k is the Boltzmann constant, T is the absolute temperature, and q is the unit charge. For FTO/PEIE-based PSCs, the slope was dramatically decreased to 1.33 kT/q, which indicated the suppressed trap-assisted recombination in the PSCs [37]. As shown in Figure 2, a PEIE coating could reduce the surface roughness of FTO, which is beneficial for suppressing the formation of defects in the PSCs [31]. As a result, the defect-induced charge traps would be decreased when using PEIE, which is consistent with the analysis of V_{oc} dependence.

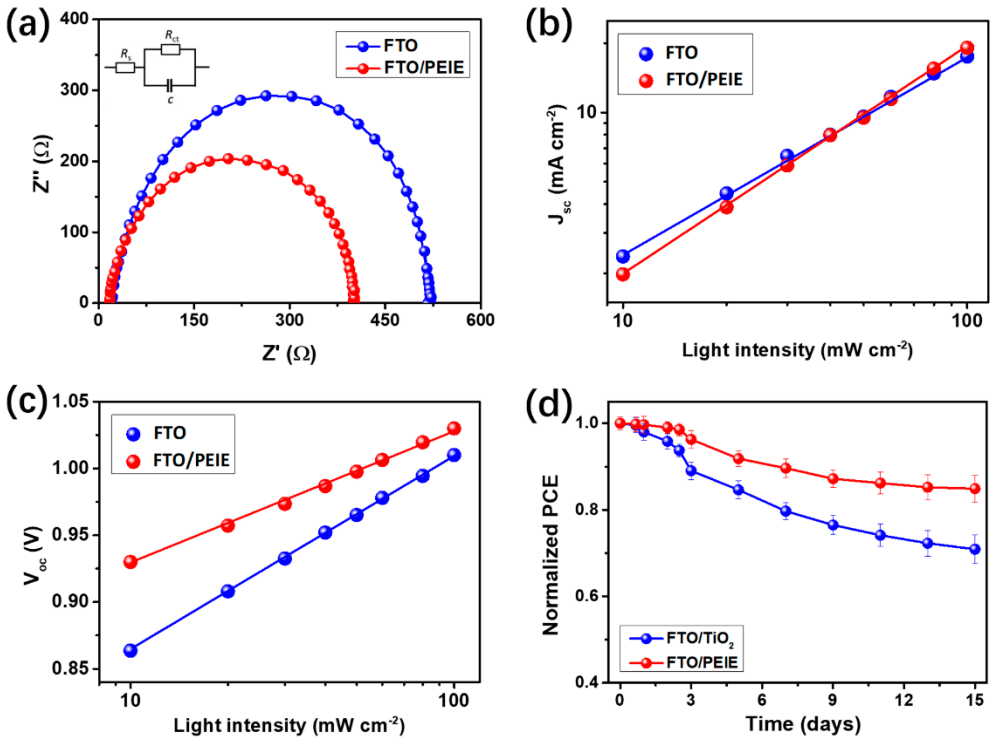

Figure 6. (**a**) EIS spectra of the PSCs fabricated on bare FTO and FTO/PEIE substrates; Light intensity dependence of J_{sc} (**b**) and V_{oc} (**c**) for PSCs using bare FTO and FTO/PEIE as the cathodes (**d**) Long-term stability performance of the PSCs fabricated on FTO/PEIE and FTO/TiO_2 substrates, in terms of the normalized PCE vs. time.

Additionally, we tested the long-term stability of the FTO/PEIE-based ETL-free and TiO_2-based regular PSCs for 15 days with results shown in Figure 6d. The samples were stored and measured in ambient conditions (at about 25 °C, 35% relative humidity) without encapsulation. After 15 days, the TiO_2-based regular PSCs only retained a final PCE of 9.6%, indicating a fast PCE degradation of about 29% (initial PCE = 13.5%). However, the FTO/PEIE-based ETL-free PSCs exhibited a higher remaining PCE of 10.6% after the measurement, corresponding to a slow PCE degradation of about 16%. The degraded performance of the PSCs could be due to the decomposition of $(BA)_2(MA)_3Pb_4I_{13}$ perovskite films [38,39]. As indicated from previous studies, TiO_2 has a photocatalytic effect on

perovskite with irradiation of UV light, leading to a gradual decomposition of perovskite into PbI_2 [13]. For the ETL-free PSCs without using TiO_2, the catalysis-induced perovskite degradation can be avoided. As a result, the significantly improved stability is another advantage for the ETL-free PSCs using FTO/PEIE as the cathode.

4. Conclusions

In conclusion, we developed a PEIE-coated FTO electrode for the fabrication of ETL-free Ruddlesden–Popper 2D PSCs. With the deposition of a thin PEIE layer, work function of the FTO electrode was tuned from −4.72 to −4.08 eV, which is induced by the formation of surface dipoles. The improved alignment of energy bands is beneficial for electron extraction from the perovskite absorber. Consequently, the PSCs fabricated on FTO/PEIE substrates exhibited an average PCE of 12.7%, which is much higher than that of PSCs on bare FTO (9.6%). The analysis of light absorption, XRD, and SEM measurements indicated the high quality of the prepared $(BA)_2(MA)_3Pb_4I_{13}$ perovskite film on FTO/PEIE substrates. The PL, TR-PL, EIS, and light-intensity-dependent analysis demonstrate the improved electron transport property in the PSCs when coating PEIE onto FTO. Compared with conventional TiO_2-based PSCs (with PCE = 13.5%), although the ETL-free PSCs showed slightly lower PCE, the total fabricating temperature of the devices was dramatically lowered from 500 to 100 °C. Moreover, the long-term stability of the PSCs was significantly improved for a duration of 15 days in ambient conditions. The PCE degradation of the ETL-free PSCs is only 16%, whereas the TiO_2-based PSCs showed a high PCE degradation of 29%. The best PSC using FTO/PEIE cathode exhibits a highest PCE of 13.0%, with a stable power output and a low hysteresis degree. Our results demonstrate that PEIE modified FTO is a good electron collecting electrode for realizing high-performance ETL-free 2D PSCs.

Supplementary Materials: The following supporting information can be downloaded at https://www.mdpi.com/article/10.3390/cryst12081090/s1. Figure S1: Contact angle measurements of (a) bare FTO and (b) PEIE coated FTO substrates; Figure S2: *J*–*V* characteristics of the PSCs using TiO_2 as the ETL; Figure S3: PCE trend with standard deviations for PSCs fabricated on bare FTO, FTO/PEIE and FTO/TiO_2 substrates.

Author Contributions: Conceptualization, Z.L.; methodology and formal analysis, H.Z. and L.W.; investigation and writing, N.D.; review and editing, all authors; supervision, Z.L. All authors have read and agreed to the published version of the manuscript.

Funding: This work was financially supported by the Yantai University Doctoral Start-up Fund (No.: WL18B23).

Data Availability Statement: Not applicable.

Acknowledgments: The authors are thankful to Xuewen Liu and Binghui Li for providing technical support. The authors specially thank the Department of Physics, Yantai University, for providing the needed instruments for measurements.

Conflicts of Interest: There are no conflict to declare.

References

1. Lee, M.M.; Teuscher, J.; Miyasaka, T.; Murakami, T.N.; Snaith, H.J. Efficient Hybrid Solar Cells Based on Meso-Superstructured Organometal Halide Perovskites. *Science* **2012**, *338*, 643–647. [CrossRef]
2. Yang, W.S.; Park, B.-W.; Jung, E.H.; Jeon, N.J.; Kim, Y.C.; Lee, D.U.; Shin, S.S.; Seo, J.; Kim, E.K.; Noh, J.H.; et al. Iodide Management in Formamidinium-Lead-Halide–based Perovskite Layers for Efficient Solar Cells. *Science* **2017**, *356*, 1376–1379. [CrossRef] [PubMed]
3. Shi, D.; Adinolfi, V.; Comin, R.; Yuan, M.; Alarousu, E.; Buin, A.; Chen, Y.; Hoogland, S.; Rothenberger, A.; Katsiev, K.; et al. Low Trap-State Density and Long Carrier Diffusion in Organolead Trihalide Perovskite Single Crystals. *Science* **2015**, *347*, 519–522. [CrossRef] [PubMed]
4. Kojima, A.; Teshima, K.; Shirai, Y.; Miyasaka, T. Organometal Halide Perovskites as Visible-Light Sensitizers for Photovoltaic Cells. *J. Am. Chem. Soc.* **2009**, *131*, 6050–6051. [CrossRef] [PubMed]
5. NREL Best Research-Cell Efficiency Chart (Photovoltaic Research). Available online: https://www.nrel.gov/pv/cell-efficiency.html (accessed on 30 June 2022).

6. Hu, Y.; Qiu, T.; Bai, F.; Miao, X.; Zhang, S. Enhancing Moisture-Tolerance and Photovoltaic Performances of FAPbI3 by Bismuth Incorporation. *J. Mater. Chem. A* **2017**, *5*, 25258–25265. [CrossRef]
7. Christians, J.A.; Miranda Herrera, P.A.; Kamat, P.V. Transformation of the Excited State and Photovoltaic Efficiency of $CH_3NH_3PbI_3$ Perovskite upon Controlled Exposure to Humidified Air. *J. Am. Chem. Soc.* **2015**, *137*, 1530–1538. [CrossRef] [PubMed]
8. Tsai, H.; Nie, W.; Blancon, J.-C.; Stoumpos, C.C.; Asadpour, R.; Harutyunyan, B.; Neukirch, A.J.; Verduzco, R.; Crochet, J.J.; Tretiak, S.; et al. High-Efficiency Two-Dimensional Ruddlesden–Popper Perovskite Solar Cells. *Nature* **2016**, *536*, 312–316. [CrossRef]
9. Cao, D.H.; Stoumpos, C.C.; Farha, O.K.; Hupp, J.T.; Kanatzidis, M.G. 2D Homologous Perovskites as Light-Absorbing Materials for Solar Cell Applications. *J. Am. Chem. Soc.* **2015**, *137*, 7843–7850. [CrossRef] [PubMed]
10. Kim, H.; Lim, K.-G.; Lee, T.-W. Planar Heterojunction Organometal Halide Perovskite Solar Cells: Roles of Interfacial Layers. *Energy Environ. Sci.* **2016**, *9*, 12–30. [CrossRef]
11. Wang, P.-C.; Govindan, V.; Chiang, C.-H.; Wu, C.-G. Room-Temperature-Processed Fullerene/TiO_2 Nanocomposite Electron Transporting Layer for High-Efficiency Rigid and Flexible Planar Perovskite Solar Cells. *Solar RRL* **2020**, *4*, 2000247. [CrossRef]
12. Kogo, A.; Sanehira, Y.; Ikegami, M.; Miyasaka, T. Brookite TiO_2 as a Low-Temperature Solution-Processed Mesoporous Layer for Hybrid Perovskite Solar Cells. *J. Mater. Chem. A* **2015**, *3*, 20952–20957. [CrossRef]
13. Leijtens, T.; Eperon, E.; Pathak, S.; Abate, A.; Lee, M.M.; Snaith, H.J. Overcoming Ultraviolet Light Instability of Sensitized TiO_2 with Meso-Superstructured Organometal Tri-Halide Perovskite Solar Cells. *Nat. Commun.* **2013**, *4*, 2885. [CrossRef]
14. Jiang, Q.; Zhang, L.; Wang, H.; Yang, X.; Meng, J.; Liu, H.; Yin, Z.; Wu, J.; Zhang, X.; You, J. Enhanced Electron Extraction Using SnO_2 for High-Efficiency Planar-Structure HC(NH2)2PbI3-based Perovskite Solar Cells. *Nat. Energy* **2017**, *2*, 16177. [CrossRef]
15. Luo, J.; Wang, Y.; Zhang, Q. Progress in Perovskite Solar Cells based on ZnO nanostructures. *Sol. Energy* **2018**, *163*, 289–306. [CrossRef]
16. Zhang, P.; Wu, J.; Zhang, T.; Wang, Y.; Liu, D.; Chen, H.; Ji, L.; Liu, C.; Ahmad, W.; Chen, Z.D.; et al. Perovskite Solar Cells with ZnO Electron-Transport Materials. *Adv. Mater.* **2018**, *30*, 1703737. [CrossRef] [PubMed]
17. Wojciechowski, K.; Leijtens, T.; Siprova, S.; Schlueter, C.; Hörantner, M.T.; Wang, J.T.-W.; Li, C.-Z.; Jen, A.K.-Y.; Lee, T.-L.; Snaith, H.J. C60 as an Efficient n-Type Compact Layer in Perovskite Solar Cells. *J. Phys. Chem. Lett.* **2015**, *6*, 2399–2405. [CrossRef]
18. Zhang, M.; Zhu, J.; Liu, K.; Zheng, G.; Zhao, G.; Li, L.; Meng, Y.; Guo, T.; Zhou, H.; Zhan, X. A Low Temperature Processed Fused-Ring Electron Transport Material for Efficient Planar Perovskite Solar Cells. *J. Mater. Chem. A* **2017**, *5*, 24820–24825. [CrossRef]
19. Huang, L.; Hu, Z.; Xu, J.; Sun, X.; Du, Y.; Ni, J.; Cai, H.; Li, J.; Zhang, J. Efficient Electron-Transport Layer-Free Planar Perovskite Solar Cells via Recycling the FTO/Glass Substrates from Degraded Devices. *Sol. Energy Mater. Sol. Cells* **2016**, *152*, 118–124. [CrossRef]
20. Huang, S.; Dong, Q.; Lu, Y.; Duan, L.; Zhang, D. Outstanding Performance of Electron-Transport-Layer-Free Perovskite Solar Cells Using a Novel Small-Molecule Interlayer Modified FTO Substrate. *Chem. Eng. J.* **2021**, *422*, 130001. [CrossRef]
21. Wu, W.-Q.; Liao, J.-F.; Zhong, J.-X.; Xu, Y.-F.; Wang, L.; Huang, J. Suppressing Interfacial Charge Recombination in Electron-Transport-Layer-Free Perovskite Solar Cells to Give an Efficiency Exceeding 21%. *Angew. Chem. Int. Ed.* **2020**, *59*, 20980–20987. [CrossRef]
22. Zhang, P.; Zhang, T.; Wang, Y.; Liu, D.; Xu, H.; Chen, L.; Li, Y.; Wu, J.; Chen, Z.D.; Li, S. Enhanced Thermal Stability of Electron Transport Layer-Free Perovskite Solar Cells via Interface Strain Releasing. *J. Power Sources* **2019**, *439*, 227091. [CrossRef]
23. Chen, L.; Xie, X.; Liu, Z.; Lee, E.-C. A Transparent Poly(3,4-Ethylenedioxylenethiophene):Poly(Styrene Sulfonate) Cathode for Low Temperature Processed, Metal-Oxide Free Perovskite Solar Cells. *J. Mater. Chem. A* **2017**, *5*, 6974–6980. [CrossRef]
24. Liu, Y.; Liu, Z.; Lee, E.-C. High-Performance Inverted Perovskite Solar Cells Using Doped Poly(triarylamine) as the Hole Transport Layers. *ACS Appl. Energy Mater.* **2019**, *2*, 1932–1942. [CrossRef]
25. Liu, Z.; Wang, L.; Xu, C.; Xie, X. Electron-Transport-Layer-Free Two-Dimensional Perovskite Solar Cells based on a Flexible Poly(3,4-ethylenedioxythiophene):Poly(styrenesulfonate) Cathode. *Sustain. Energy Fuels* **2021**, *5*, 2595–2601.
26. Zhou, Y.; Fuentes-Hernandez, C.; Shim, J.; Meyer, J.; Giordano, A.J.; Li, H.; Winget, P.; Papadopoulos, T.; Cheun, H.; Kim, J.; et al. A Universal Method to Produce Low-Work Function Electrodes for Organic Electronics. *Science* **2012**, *336*, 327–332. [CrossRef]
27. Xu, C.; Liu, Z.; Sun, Q.; Lee, E.-C. Morphology Control of SnO_2 Layer by Solvent Engineering for Efficient Perovskite Solar Cells. *Sol. Energy* **2021**, *214*, 280–287. [CrossRef]
28. Zhang, X.; Ren, X.; Liu, B.; Munir, R.; Zhu, X.; Yang, D.; Li, J.; Liu, Y.; Smilgies, D.; Li, R.; et al. Stable High Efficiency Two-Dimensional Perovskite Solar Cells via Cesium Doping. *Energy Environ. Sci.* **2017**, *10*, 2095–2102. [CrossRef]
29. Liu, Z.; Wang, L.; Xie, X. Improving the Performance of Inverted Two-Dimensional Perovskite Solar Cells by Adding an Anti-Solvent into the Perovskite Precursor. *J. Mater. Chem. C* **2020**, *8*, 11882–11889.
30. He, T.; Li, S.; Jiang, Y.; Qin, C.; Cui, M.; Qiao, L.; Xu, H.; Yang, J.; Long, R.; Wang, H.; et al. Reduced-Dimensional Perovskite Photovoltaics with Homogeneous Energy Landscape. *Nat. Commun.* **2020**, *11*, 1672. [CrossRef] [PubMed]
31. Liu, Z.; Wang, L.; Xie, X.; Xu, C.; Tang, J.; Li, W. High-Performance Ruddlesden-Popper Two-Dimensional Perovskite Solar Cells via Solution Processed Inorganic Charge Transport Layers. *Phys. Chem. Chem. Phys.* **2022**, *24*, 15912–15919. [CrossRef]

32. Xia, F.; Wu, Q.; Zhou, P.; Li, Y.; Chen, X.; Liu, Q.; Zhu, J.; Dai, S.; Lu, Y.; Yang, S. Efficiency Enhancement of Inverted Structure Perovskite Solar Cells via Oleamide Doping of PCBM Electron Transport Layer. *ACS Appl. Mater. Interfaces* **2015**, *7*, 13659–13665. [CrossRef] [PubMed]
33. Xu, C.; Liu, Z.; Lee, E.-C. Stability and Efficiency Improved Perovskite Solar Cells through Tuning the Hydrophobicity of the Hole Transport Layer with an Organic Semiconductor. *J. Mater. Chem. C* **2021**, *9*, 679–686. [CrossRef]
34. Rodriguez-Romero, J.; Hames, B.C.; Mora-Seró, I.; Barea, E.M. Conjugated Organic Cations to Improve the Optoelectronic Properties of 2D/3D Perovskites. *ACS Energy Lett.* **2017**, *2*, 1969–1970. [CrossRef]
35. Rodriguez-Romero, J.; Sanchez-Diaz, J.; Echeverria-Arrondo, C.; Masi, S.; Esparza, D.; Barea, E.M.; Mora-Seró, I. Widening the 2D/3D Perovskites Family for Efficient and Thermal-Resistant Solar Cells by the Use of Secondary Ammonium Cations. *ACS Energy Lett.* **2020**, *5*, 1013–1021. [CrossRef]
36. Yang, D.; Zhou, X.; Yang, R.; Yang, Z.; Yu, W.; Wang, X.; Li, C.; Liu, S.; Chang, R.P.H. Surface Optimization to Eliminate Hysteresis for Record Efficiency Planar Perovskite Solar Cells. *Energy Environ. Sci.* **2016**, *9*, 3071–3078. [CrossRef]
37. Liu, Z.; Xie, X.; Liu, G.; Lee, E.-C. High-Performance Metal-Oxide-Free Perovskite Solar Cells based on Organic Electron Transport Layer and Cathode. *Org. Electron.* **2019**, *64*, 195–201. [CrossRef]
38. Liu, Z.; Wang, L.; Xu, C.; Xie, X.; Zhang, Y. Hole-Tranport-Underlayer-Induced Crystallization Management of Two-Dimensional Perovskite for High-Performance Inverted Solar Cells. *ACS Appl. Energy Mater.* **2021**, *4*, 10574–10583. [CrossRef]
39. Wang, R.; Mujahid, M.; Duan, Y.; Wang, Z.-K.; Xue, J.; Yang, Y. A Review of Perovskite Solar Cell Stability. *Adv. Funct. Mater.* **2019**, *29*, 1808843. [CrossRef]